Research Square

Preprints are preliminary reports that have not undergone peer review.
They should not be considered conclusive, used to inform clinical practice,
or referenced by the media as validated information.

Tailoring the physicochemical properties of Monolayer MoS_2 through Ion Beam-Controlled Thiol Functionalization

Francesco Laudani
TU Wien
Florian Fahrnberger
TU Wien
Markus Sauer
TU Wien
Markus Ostermann
TU Wien
Markus Valtiner
TU Wien
Annette Foelske
annette.foelske@tuwien.ac.at

TU Wien

Article

Keywords:

Posted Date: November 25th, 2026

DOI: https://doi.org/10.21203/rs.3.rs-11718417/v1

License: This work is licensed under a Creative Commons Attribution 4.0 International License.
Read Full License

Additional Declarations: No competing interests reported.

Tailoring the physicochemical properties of Monolayer MoS_2 through Ion Beam-Controlled Thiol Functionalization

Francesco Laudani[a], Florian Fahrnberger[a], Markus Sauer[a], Markus Ostermann[b], Markus Valtiner[b], and Annette Foelske[a]**

[a]*Analytical Instrumentation Center, TU Wien, Vienna 1060, Austria*

[b]*Applied Interface Physics, TU Wien, Vienna 1040, Austria*

**e-mail: francesco.laudani@tuwien.ac.at, annette.foelske@tuwien.ac.at*

Abstract

Monolayer molybdenum disulfide (MoS_2) offers opportunities for electronics and sensing, but the low reactivity of its pristine basal plane limits direct surface functionalization. Here, we demonstrate that low-energy Ar ion irradiation enables controlled thiol functionalization of Au-supported monolayer MoS_2 by generating sulfur-deficient, undercoordinated Mo environments whose abundance increases with ion fluence. X-ray photoelectron spectroscopy (XPS) reveals that these irradiation-generated sites enhance ambient oxidation as well as reactivity towards 1H,1H,2H,2H-perfluorodecanethiol (PFDT). Because irradiation can partially remove the monolayer and expose the underlying Au, an attenuation-based XPS model was developed to estimate and subtract the contribution from PFDT self-assembled monolayers formed on uncovered Au regions. After correction, the MoS_2-associated fluorine signal, used as a relative measure of functionalization density, increases by up to (4.8 ± 0.6) times compared with untreated monolayers. The functionalized samples remain stable without detectable oxidation after more than one month in air, supporting effective passivation of irradiation-generated reactive sites. Kelvin probe force microscopy further reveals a systematic increase in relative work function with functionalization density. These findings establish ion-beam-controlled

functionalization as a patternable route for tailoring the chemical and physical properties of monolayer MoS_2.

Introduction Monolayer molybdenum disulfide, MoS_2, is one of the most widely studied two-dimensional transition-metal dichalcogenides because it combines atomic-scale thickness with a semiconducting electronic structure, chemical robustness, and compatibility with device architectures. In contrast to bulk MoS_2, which has an indirect band gap, the monolayer possesses a direct band gap of approximately 1.8-1.9 eV, making it attractive for field-effect transistors, photodetectors, optoelectronic devices, and chemical sensors [1–4]. For sensing applications in particular, the entire active channel is exposed to the environment, so adsorption or chemical modification at the surface can strongly affect charge density, carrier scattering, or photoluminescence [5–7]. High surface sensitivity is advantageous, but it also creates a central challenge: pristine MoS_2 can respond to many adsorbates, yet its chemical selectivity is often limited unless the surface is functionalized with chemically specific binding sites. Surface functionalization of MoS_2 is therefore an important route toward selective sensors and chemically tailored devices. However, functionalization is constrained by the relatively low reactivity of the basal plane. In ideal 2H-MoS_2, the basal surface is terminated by fully coordinated sulfur atoms and lacks dangling bonds [8,9]. By contrast, edges, grain boundaries, and point defects contain undercoordinated atoms and are much more chemically active[10,11]. Among the point defects present in monolayer MoS_2, sulfur vacancies are especially important. Transmission electron microscopy (TEM) and scanning probe microscopy (SPM) studies have shown that sulfur vacancies and related vacancy complexes are common native defects in mechanically exfoliated and chemically grown monolayers [12–15]. Theoretical and experimental studies further indicate that these vacancies introduce localized electronic states and expose coordinatively unsaturated molybdenum atoms, thereby increasing the affinity of the basal plane toward molecular adsorbates, oxygen-containing species, and chemical functional groups

[16–18]. Consequently, sulfur vacancies can be viewed not only as electronic defects, but also as chemically active sites. This concept has motivated a broad range of defect-engineering approaches aimed at activating the basal plane of MoS_2 while preserving the overall two-dimensional lattice. Several methods have been developed to introduce defects into MoS_2, including plasma exposure, electron irradiation, thermal or vacuum annealing, chemical treatment, and ion irradiation [17,19–21]. For supported monolayers, ion beam-induced reactivity is particularly appealing because it enables direct patterning without conventional lithography, making it a solvent-free approach that can reduce the number of processing steps. Ion beam exposure can preferentially remove sulfur atoms and generate vacancy-type defects, but at high fluences, defect-defect interactions, vacancy clustering, amorphization, or loss of long-range structural integrity become increasingly important [22–25]. Therefore, ion beam treatment offers a practical way to vary the defect density, but it also requires care to distinguish controlled chemical activation from irreversible structural damage. Our previous study on ion beam-induced desulfurization of bulk and monolayer MoS_2 showed that it is possible to achieve controlled desulfurization over a range of fluences while preserving molybdenum from removal [26]. These results raised a direct question that motivates the present work: can the physicochemical properties of monolayer MoS_2 be tailored systematically by tuning the density of ion beam-generated sulfur vacancies? To investigate this, we used X-ray Photoelectron Spectroscopy (XPS) as the main investigation technique. This choice is central to the study because the question requires not only detecting which elements are present but also distinguishing their chemical environments. XPS provides this combination of elemental and chemical-state sensitivity in a quantitative to semiquantitative framework, making it possible to compare changes in relative elemental quantities, molybdenum chemical state, oxidation products, and molecular markers within the same experimental approach. Its high surface sensitivity is particularly important for monolayer MoS_2, where the relevant chemical processes occur at the basal plane rather than in a bulk volume.

At the same time, XPS probes micrometer-scale regions of the flake, giving an averaged chemical response from extended monolayer areas rather than from isolated point defects. This is especially useful for ion-beam-treated samples, where the relevant variable is the average defect density produced by a given fluence. The XPS results were complemented by using Raman spectroscopy to follow structural modifications induced by the ion beam treatment process, and by Kelvin Probe Force Microscopy to assess the tunability of the material's physical properties. We started by probing the quantitative effects of different ion pre-treatment fluences on the material's reactivity by monitoring its oxidation in ambient air. The oxidation behavior of MoS_2 shows a kinetic distinction between pristine and defective regions. MoO_3 is, under ambient conditions, more thermodynamically stable than the respective sulfide. Under oxygen-rich conditions, oxidative conversion of MoS_2 is in principle favorable. Nevertheless, the basal plane of high-quality MoS_2 is relatively stable in ambient conditions because oxidation is kinetically hindered at room temperature. Oxidation becomes much more efficient at defective sites, and it can be accelerated by thermal treatment, light, plasma exposure, ozone, or other activating conditions [27,28]. Recent work has shown that oxygen can substitute sulfur-vacancy sites or bind at vacancy-related defects, changing both the chemical state and the electronic properties of monolayer MoS_2 [29–31]. In addition to oxidation, thiol chemistry provides a second and complementary test of defect-mediated reactivity. Sulfur-containing organic molecules are attractive for functionalizing MoS_2 because thiol or thiolate groups can interact with undercoordinated molybdenum atoms and may passivate or occupy sulfur-vacancy sites, while the organic tail can be chosen to introduce specific chemical functionality [32–36]. Fluorinated thiols are particularly useful molecular probes in this context. Their thiol group can target defect-related reactive sites, while the fluorinated tail provides an element-specific XPS marker through the F 1s core level. Performing the thiol reaction under inert glove-box conditions further separates intrinsic defect-mediated functionalization from uncontrolled oxidation by ambient air. Here, we investigate how the chemical

reactivity of supported monolayer MoS_2 changes as a function of ion beam fluence. A series of Au-supported monolayer MoS_2 samples is exposed to different ion fluences to generate different levels of sulfur deficiency. The resulting reactivity is then probed by two distinct chemical reactions: exposure to ambient air tests the susceptibility of the defective basal plane toward oxidation, while reaction with a fluorinated thiol allows investigation of the ability of vacancy-type defects to promote molecular functionalization.

Results and Discussion

Ion beam exposure Three ion fluences were selected to investigate the effect of defect density on reactivity: 5.0×10^{13}, 7.5×10^{13}, and 1.00×10^{14} ions/cm^2. The fluences were chosen to be in a range that causes detectable sulfur depletion, while avoiding substantial removal of the layer. A depth profile was performed on a sample to estimate the sulfur loss. Considering the chosen fluences, from the lowest to the highest, the respective percentages of removed sulfur are (14.0 ± 0.5) %, (21.0 ± 0.75) %, and (28.0 ± 1.0) %. (For details of the estimation method, refer to SI). Figure 1a shows the XPS Mo 3d spectra acquired before and after ion beam exposure. Pristine MoS_2 monolayer on Au shows asymmetric Mo 3d, S 2p, and S 2s peaks; by comparison with multilayer MoS_2/Au, Velický et al. [37] showed that marked asymmetry is reported only for the monolayer. The asymmetry has been investigated by Hanušová et al. [38], and it has been attributed to orbital hybridization between MoS_2 and the underlying metal. The study shows the asymmetry to be a result of the interaction between the bottom sulfur layer and the substrate. The figure also shows that ion beam exposure induces a shift of the Mo 3d peak towards lower binding energies and a tail at low binding energies in the peak shape of Mo 3d signals. Because the system consists of a single Mo layer (represented in Figure 1b), the spectra were analyzed using a two-component areal-fraction model (for details, refer to our previous study [26]).

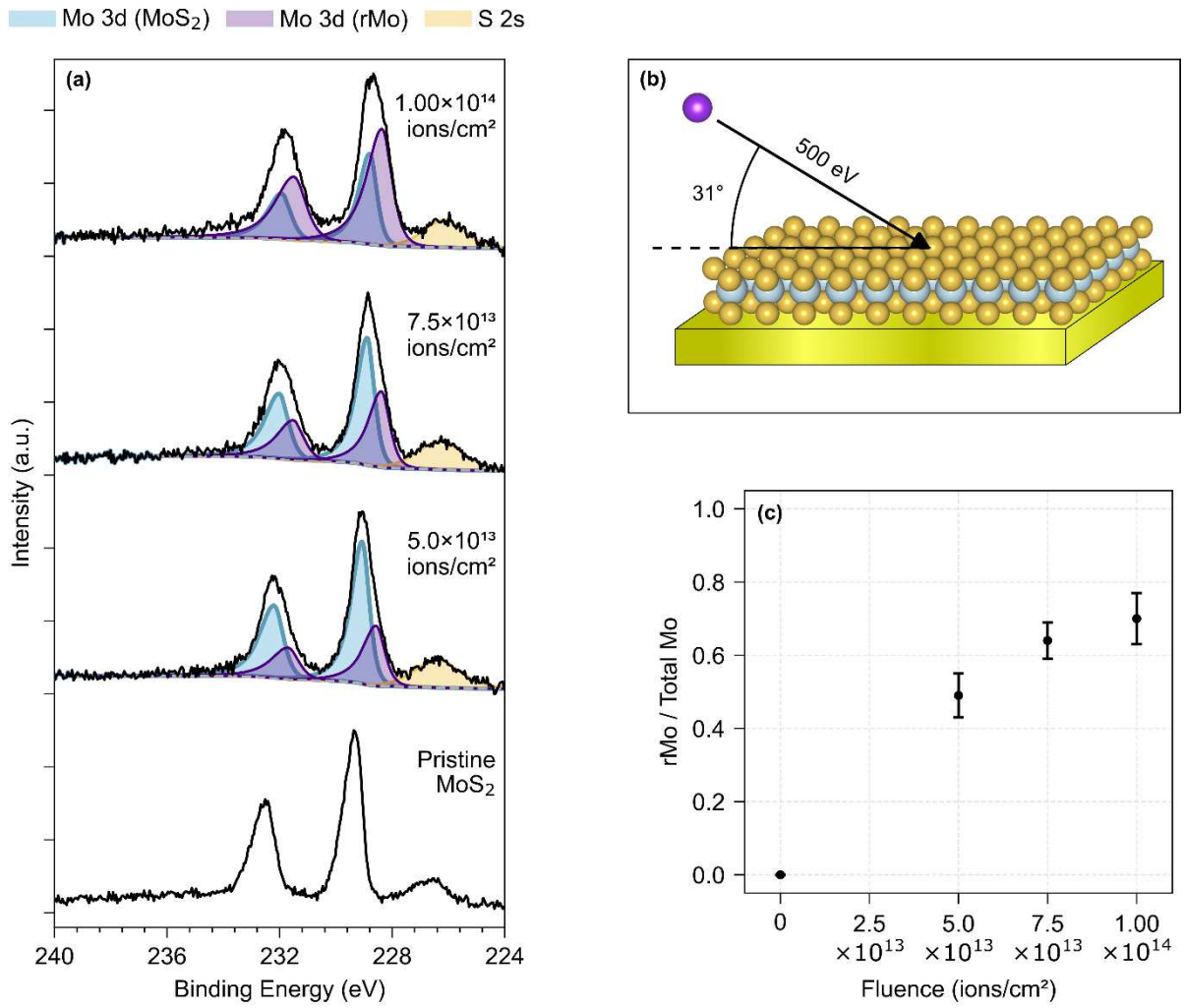

Figure 1 – (a) Mo 3d spectra of the MoS_2 monolayer on Au before and after treatment with each investigated fluence of ion beam exposure. Peak fitting shows pristine MoS_2 (Cyan), reduced molybdenum rMo (Purple), and S 2s (Orange). (b) Schematic representation of the ion beam treatment process. (c) Impact of the fluence on the relative amount of undercoordinated molybdenum (rMo / Total Mo). Error bars represent the standard deviation across all the ion beam-treated samples used in the study at the respective fluence.

Briefly, the first component represents Mo atoms that are not affected by ion irradiation and are therefore assigned to the pristine MoS_2 phase. This component was fitted using the same full width at half maximum (FWHM) as that obtained from the pristine sample spectra. The second component accounts for Mo atoms whose local coordination environment has been modified by sulfur removal; this contribution is attributed to reduced molybdenum (rMo). This fitting approach and the physical

129 interpretation of the rMo component were established and explained more extensively in our
130 previous study on ion beam exposure of MoS_2 [26]. This evolution is particularly relevant to the chemical
131 reactivity of the material, since the rMo contribution is attributed to sulfur-deficient Mo sites, which
132 are expected to act as the primary reactive centers. Figure 1c shows that the fractional amount of
133 reduced molybdenum reaches values of around 0.5 for the lowest fluence up to 0.7 for the highest
134 fluence applied in our study. At first glance, these values may seem extremely overestimated, but
135 considering the coordination environment of MoS_2, the removal of one sulfur atom leads to three
136 undercoordinated molybdenum atoms [39]. The average percentage of reduced molybdenum results in
137 fact to be around three times higher than the respective estimated sulfur loss for each fluence.

138 Oxidation The XPS Mo 3d, S 2p, and O1s spectra represented in Figure 2a-c show the chemical
139 changes of the monolayer at 24 hours of air exposure after being treated with the investigated ion
140 fluences. The Mo 3d shows a marked growth in the molybdenum oxide component, which is clearly
141 visible in the new components at 232. 5 and 235.6 eV, and confirmed by O 1s spectra, which increase
142 in intensity with increasing fluence, further supporting that the applied fluence may be a relevant
143 parameter for the growth rate of a molybdenum oxide (MoO_x) phase.

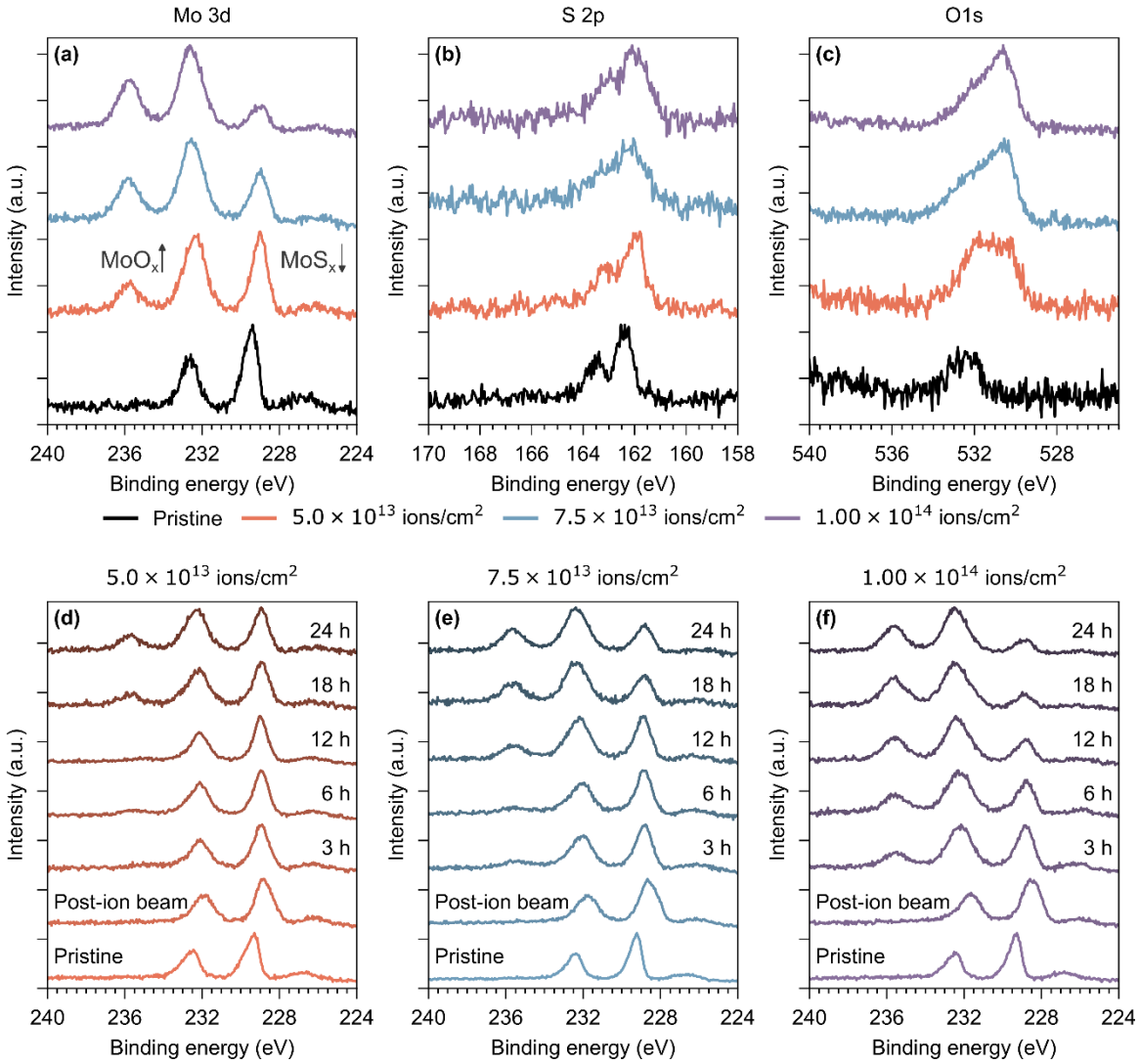

Figure 2 – Changes of Mo 3d (a), S 2p (b), and O 1s (c) XPS spectra of a monolayer MoS_2 after ion beam treatment and subsequent storage for 24 hours in ambient air. (d, e, f) Mo 3d XPS spectra before, after ion beam treatment, and at different air exposure times.

S 2p peaks do not show significant differences, apart from a signal decrease, consistent with the oxidation of the sulfide to volatile SO_2 species [28]. O 1s spectra show an increase in the low binding energy component of the peak, associated with molybdenum oxide [40]. The progressive change in the molybdenum spectra represented in Figure 2d-f shows that after the reaction starts, the peaks shift to higher binding energies and become narrower by losing the tail at lower binding energy, meaning that the rMo component is no longer visible. This could be interpreted as the reaction of

undercoordinated molybdenum with oxygen, but the percentage of oxidized molybdenum is lower than the previous percentage of undercoordinated molybdenum before the oxidation reaction. Our hypothesis is that the unreacted rMo shifts to a higher binding energy, becoming indistinguishable from the MoS_2 component. The shift might not be interpreted as a chemical state evolution, but rather as a local work function modification due to the partial filling of undercoordinated sites. The work function of the monolayer impacts the position of the peaks due to the fact that the MoS_2 / Au interface consists of a Schottky junction and therefore is subject to band bending [26,41].

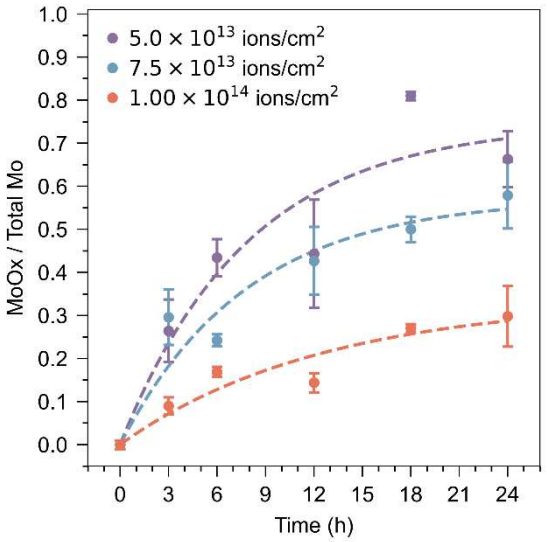

Figure 3 – Ambient air oxidation time dependence of monolayer MoS_2 after different ion beam exposure fluences. Higher fluences, associated with the formation of a higher density of reactive sites, lead to increased oxidation rates. Dotted lines represent trend lines. Error bars represent the standard deviation across three samples.

The quantification (for details of the fitting procedure, refer to the methods section) in Figure 3 shows more clearly that the oxidation time dependence changes with applied fluence. Despite the influence of different humidity levels (20% - 40%), the experimental results clearly show a trend that is compatible with Langmuir adsorption isotherms [42], as expected for a two-dimensional system. As shown in previous oxidation studies, molybdenum oxide is thermodynamically more stable than the

sulfide phase. As previously mentioned, the reason why MoS_2 can be stable in air for long periods is its kinetic stability, given by the lack of dangling bonds that act as reaction centers [10,11,43]. This means that even though the pristine material naturally presents vacancies, the low concentration of defects makes the oxidation process extremely slow. Creating sulfur vacancies on the basal plane using an ion beam significantly increases the oxidation rate. Our results suggest that oxygen doesn't just replace sulfur; in this case, the oxidation would slow down after filling the vacancies, and the curves would reach a saturation value. XPS measurements performed 20 days after air exposure show that the material fully turns into molybdenum oxide (Supplementary Figure 3). It's known that thermodynamic instability of the defected monolayer lowers the activation energy for the oxidation reaction, as reported by KC et al. [43], and increases the oxidation rate. We attribute the phenomenon we observed to a possible instability of the MoO_x/MoS_2 lateral interface at the edge of the oxidized regions, which induces progressive oxidation of the MoS_2 until it fully turns into molybdenum oxide.

Thiol exposure To study the improved reactivity towards thiols, the functionalization experiment was performed for the investigated fluences by monitoring the reaction at 3, 6, 12, and 24 hours of reaction time, using *1H,1H,2H,2H*-perfluorodecanethiol (PFDT) as an anchor molecule. The experiment was also performed on an untreated sample by exposing it to the thiol for 24 hours to quantify the relation between the relative increase in the adsorption of molecules and the treatment fluence. The experiment was performed on a batch of three untreated samples to consider both the possible random number of vacancies on different flakes and the instrumental error in the quantification.

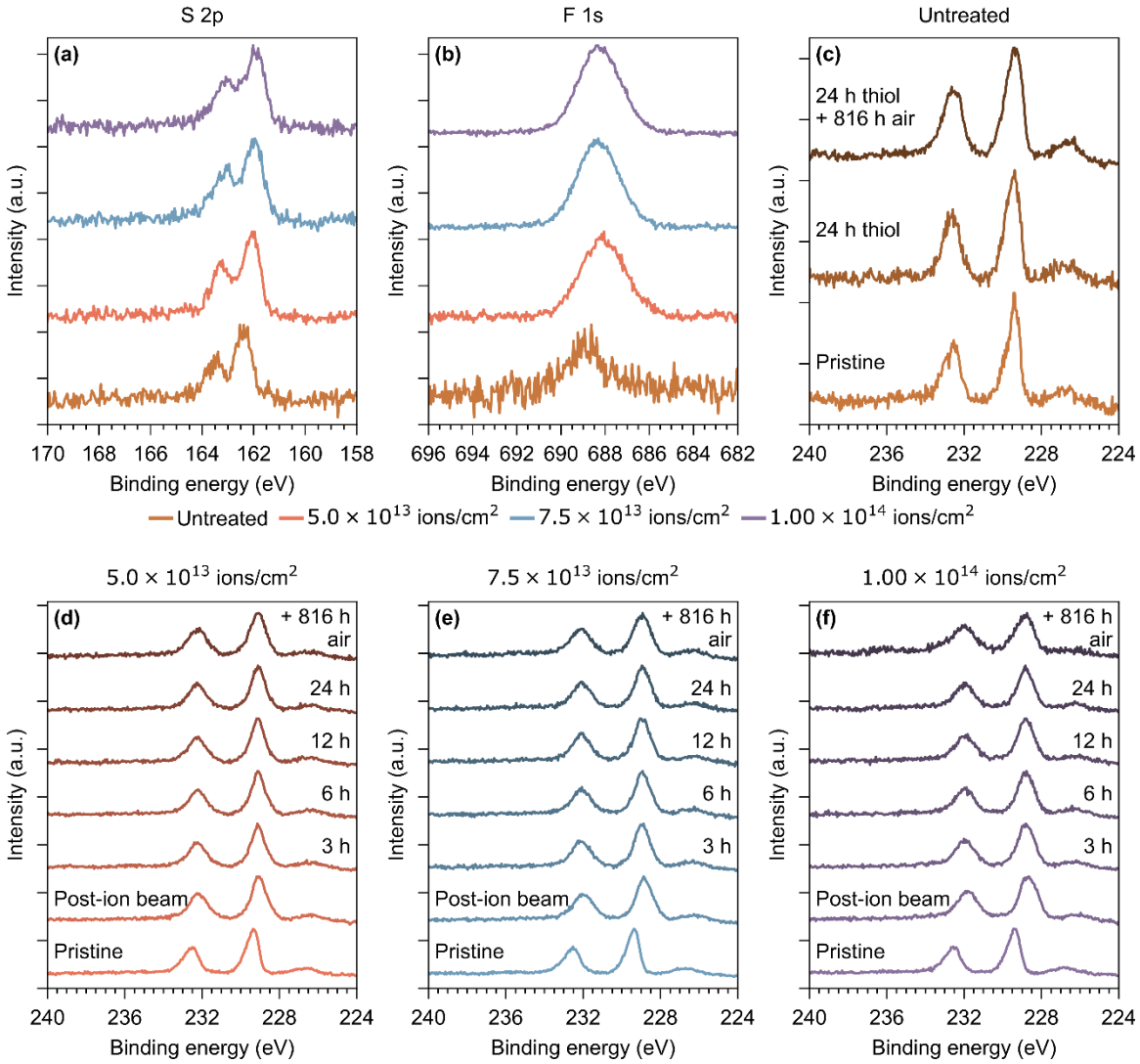

Figure 4 – Changes of S 2p (a), and F 1s (b) XPS spectra of monolayer MoS_2 at 24 hours of thiol exposure after different ion beam treatments. (c) Mo 3d XPS spectrum (d, e, f) Mo 3d XPS spectra at each step of the experiment.

The XPS spectra in Figure 4a,b show that the reaction with thiols results in the appearance of a fluorine signal, indicating the presence of adsorbed thiols on the surface. A small fluorine peak is also present in the case of the untreated monolayer; as previously mentioned, the pristine material presents a low density of native defects. S 2p peaks show small shifts to lower binding energies depending on the treatment fluence. Mo 3d spectra of the untreated samples, represented in Figure 4c, show a slight broadening of the peaks after exposure to thiols and no significant difference after

exposure to air. The broadening may be a consequence of the appearance of a thiol-bound Mo component with a chemical shift that is not large enough to resolve it from the pristine MoS_2 component. Figure 4d,e,f shows the evolution of Mo 3d spectra for the ion-treated samples. As observed for the oxidation study, the peaks get narrower after the first reaction step. We also noticed that after the reaction, Mo 3d peaks become symmetric. In agreement with the XPS analysis of Hanušová et al. [38], we attribute this increased symmetry to a modification of the electronic interaction between the monolayer and the Au substrate. Fluorine may withdraw electron density from the sulfur sites and weaken the S-Au orbital hybridization, thereby reducing the associated substrate-to-monolayer charge transfer. A previous study by Chen et al. [35] suggests that thiols may form disulfides on the surface of MoS_2. Our S 2p spectra do not present significant differences before and after the reaction, suggesting that the thiol's sulfur bonding state cannot be distinguished from the sulfide component of MoS_2. This happens either because the chemical shift is negligible or because the amount of thiol on the surface is not sufficient to produce a detectable S 2p signal, which would be reasonable considering that the beam spot size diameter was decreased from 200 µm to around 50 µm to achieve the analysis of a fully homogeneous monolayer area, reducing the sampling area and therefore the signal intensity.

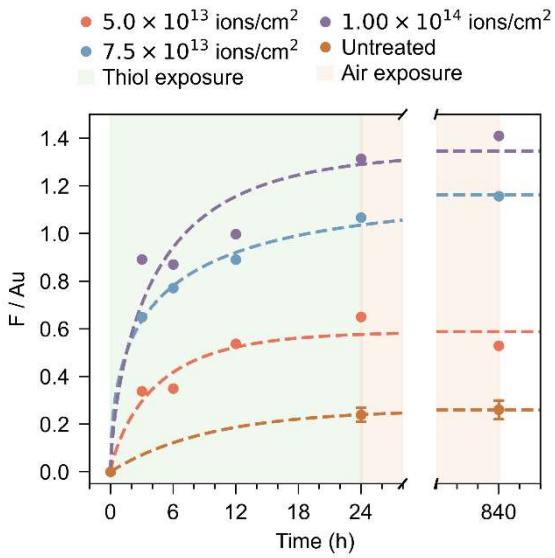

Figure 5 – Time dependence of F/Au ratio indicating the fluorine uptake on the surface (green area), and control measurements after 34 days of storage in air, at the 840 hours mark in the figure (red area). Dotted lines represent trend lines. Error bars represent the standard deviation across three samples.

The fluorine uptake on the surface is monitored by using the F/Au ratio as an index of the molecules' adsorption onto the surface. Figure 5 shows the progressive increase in the ratio with time and a clear correlation with the fluence and therefore with the density of vacancies. The uptake of sulfur, followed through the S/Au ratio (Supplementary Figure 6), also shows a trend associated with healing of vacancies. After 24 hours of reaction time, the samples were stored in air for 34 more days (840 hours in the figure) and remeasured to check for the eventual loss of functionalization due to desorption or oxidation. All of the samples showed no significant decrease in the F/Au ratio and therefore no detectable loss of functionalization over this time range. In addition, Mo 3d spectra do not show significant oxidation, supporting the hypothesis of successful functionalization. These results demonstrate effective passivation of irradiation-generated reactive sites, although the precise atomistic PFDT binding configuration is not resolved by the present XPS spectra. We note that the F/Au ratio is not fully representative of the molecule uptake. One could reasonably argue that the ion beam, apart from sulfur vacancies, creates holes in the film. This would expose Au regions, which

could be responsible for the increase in thiol uptake since thiols are well known for forming self-assembled monolayers (SAMs) on gold surfaces [44–46]. This effect, which needs to be accounted for, is responsible for part of the increase in the F/Au signal, but the data itself is not self-explanatory as to whether it's dominant or not. For this reason, a model that allows calculation of the contribution of the formation of a SAM on the exposed Au regions and decouples it from the contribution of the functionalization of MoS_2 was built. In the model, the thiols are assumed to interact only with the uncovered gold regions, forming a SAM on them. The equation describing the model is the following:

$$\frac{I_{F_{1s}}\sigma_{Au_{4f}}}{I_{Au_{4f}}\sigma_{F_{1s}}} = \frac{F}{Au}(C) = \frac{(1-C)\rho_{F,fSAM}\lambda_{F_{1s},fSAM}\left(1-e^{-\frac{t_{fSAM}}{\lambda_{F_{1s},fSAM}\,cos(\alpha)}}\right)}{(1-C)\rho_{Au}\lambda_{Au_{4f},Au}\left(e^{-\frac{t_{SAM}}{\lambda_{Au_{4f},SAM}\,cos(\alpha)}}\right)+C\rho_{Au}\lambda_{Au_{4f},Au}\left(e^{-\frac{t_{MoS_2}}{\lambda_{Au_{4f},MoS_2}\,cos(\alpha)}}\right)} \quad (Equation\ 1)$$

C = MoS_2 fractional coverage

$\rho_{F,fSAM}$ = Atomic density of fluorine in the fluorinated part of the SAM [atoms/cm^3]

$\lambda_{F1s,fSAM}$ = Effective Attenuation Length of F_{1s} photoelectrons through the fluorinated part of the SAM [nm]

t_{fSAM} = Thickness of the fluorinated part of the SAM [nm]

t_{SAM} = Thickness of the SAM layer [nm]

t_{MoS2} = Thickness of the MoS_2 monolayer [nm]

ρ_{Au} = Atomic density of gold [atoms/cm^3]

$\lambda_{Au4f,Au}$ = Effective Attenuation Length of Au_{4f} photoelectrons through the gold substrate [nm]

$\lambda_{Au4f,SAM}$ = Effective Attenuation Length of Au_{4f} photoelectrons through the SAM [nm]

$\lambda_{Au4f,MoS2}$ = Effective Attenuation Length of Au_{4f} photoelectrons through the MoS_2 monolayer [nm]

The equation consists of a numerator that accounts for the fluorine signal coming from the fluorinated layer of a PFDT SAM on uncovered gold regions and a denominator composed of two contributions: the first one being proportional to the signal of gold through the SAM, and the latter being proportional to the signal of gold through the MoS_2 monolayer. Attenuation lengths have been calculated using the study of Seah M. P. [47]: equation 14 has been used for F 1s electrons through the

fluorinated layer and for Au 4f through the SAM, and for Au 4f electrons through the substrate; equation 11 has been used for Au 4f electrons through MoS_2. The SAM's thickness has been obtained by knowing the chain length and tilt angle, using results from the studies of Frey et al. and Alves and Porter [48,49]. Consistency of the model was checked by recording XPS spectra of an uncovered gold region that underwent a 24 h reaction time following the same procedure used for the MoS_2 functionalization; the F/Au ratio has been calculated and used in equation 2 at C=0 to calculate the atomic density of fluorine in the fluorinated layer. The results show an experimental value of 5.3 x 10^{22} atoms/cm^3, in very good agreement with the theoretical value of 4.8 x 10^{22} atoms/cm^3 obtained by calculating the molecular density of the fluorinated layer of the SAM assuming hexagonal packing on Au(111), and using the literature value for the lattice parameter [49]. Despite the fact that our gold coating is polycrystalline, the difference in atomic density of the surface compared to the Au(111) surface may be considered to be negligible [50–52]. Further details on the calculation can be found in the SI. Fractional coverage of MoS_2 has been calculated using the Mo/Au ratio from post-ion beam exposure XPS spectra using equation 1. Figure 6a shows the curve of the Au-only thiol adsorption model and the experimental points obtained at a 24 hours reaction time. The following relation has been used to correct the F/Au ratio for the contribution of SAM formation on uncovered gold regions:

$$\left(\frac{F}{Au}\right)_{corrected} = \left(\frac{F}{Au}\right)_{experimental} - \left(\frac{F}{Au}\right)_{Au\ SAM\ model} \quad (Equation\ 2)$$

Figure 6b shows the experimental points for different ion beam fluence treatments, corrected by subtracting the calculated contribution originating from the chemisorption of thiols on gold and normalized by the untreated control samples. Error bars reflect the propagated uncertainty from the reference value. Since the model considers a non-zero F/Au ratio as originating from confined areas with homogeneous thickness, the contribution is assumed to be additive, as the ratio represents an areal contribution. The curve shows a significant increase in the functionalization density when the

material is treated with an ion beam to create defects that act as anchor points for the thiols. In particular, we notice that the density increases up to 4.8 ± 0.6 times compared to the untreated monolayer.

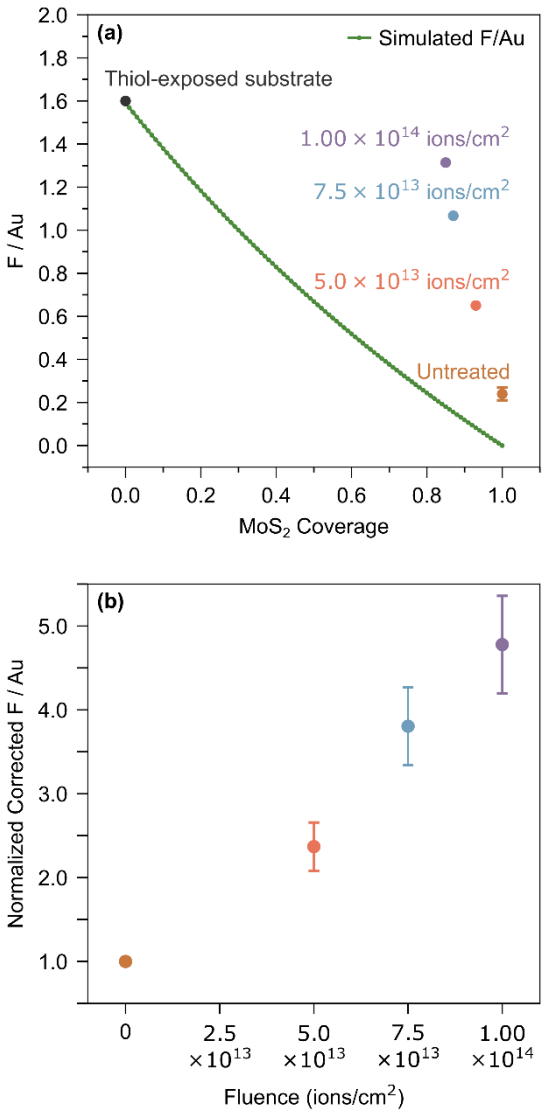

Figure 6 – Surface's uptake of molecules at 24 hours of exposure time: (a) Experimental F/Au ratios and correction model. The error bar represents the standard deviation across three samples. (b) Normalized model-corrected F/Au ratios. The quantification shows a significant increase in the uptake of molecules for increasing ion beam fluence pre-treatments. Error bars represent the propagated standard deviation of the normalization reference value.

We further performed Raman Spectroscopy on the same samples to gather additional insights on the material changes. The spectra are reported in Figure 7.

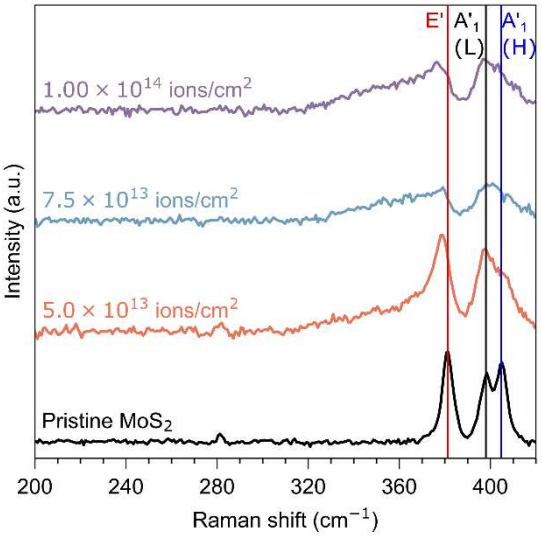

Figure 7 – Raman spectra of pristine monolayer MoS_2/Au and thiol-exposed monolayer MoS_2/Au with different ion beam pre-treatment fluences. Thiol-exposed samples have been stored in air for more than one month.

The Raman spectrum of pristine MoS_2 shows the characteristic E' and A_1' phonons, respectively associated with in-plane and out-of-plane vibrational modes. Due to the interaction with the Au substrate, the A'_1 peak undergoes splitting into the L component, associated with a stronger interaction, and the H component, associated with a weaker interaction [37,38,53]. The changes in the spectra are compared with the in situ ion beam exposure study on monolayer MoS_2 on a SiO_2 substrate by Daniel et al. and performed at fluences and energy that are comparable to our study [25]. For increasing pre-treatment fluences, the spectra show a progressive increase in features associated with loss of long-range order: decrease in intensity and broadening of the peaks, the blue shift of the E' peak, and the appearance of overlapping peaks in the region 310-360 cm^{-1} [25]. Despite the presence of these features, the LA(M) component commonly associated with the same phenomena and shown to be at around 224 cm^{-1} is not visible in our spectra [23,25]. This difference is attributed to the different substrate, since the MoS_2/Au interaction is known to modify strain, charge transfer, Raman selection

306 rules, and resonance conditions compared to SiO_2 [37,54,55]. Interestingly, the $A'_1(L)$ and the $A'_1(H)$
307 contributions decrease and broaden at different rates, with the latter being the quickest. A higher
308 $A'_1(L)/A'_1(H)$ ratio has been proven to be related to a better interaction between MoS_2 and Au [37], so
309 we hypothesize that exposure to ion beams contributes to improving the adherence of the monolayer
310 to the substrate. Supplementary Figure 7 shows the progressive increase in the FWHM of the three
311 peaks. Finally, once we established that it's possible to tune the functionalization density of the
312 material and the consequences of the ion beam treatment, we used Kelvin Probe Force Microscopy
313 in ultra-high vacuum (UHV) conditions to detect a change in the material's physical properties while
314 avoiding influence from water and physisorbed contaminants that could affect the result. In particular,
315 we measured line scans across the substrate/monolayer edge. The substrate, always consisting of Au
316 exposed to thiols for 24 hours and subject to equal air storage time, was used as a reference to track
317 the changes in the monolayer's work function and was set to a Contact Potential Difference (CPD) of
318 0 V. This allowed us to follow the relative variation in work function (Figure 8).

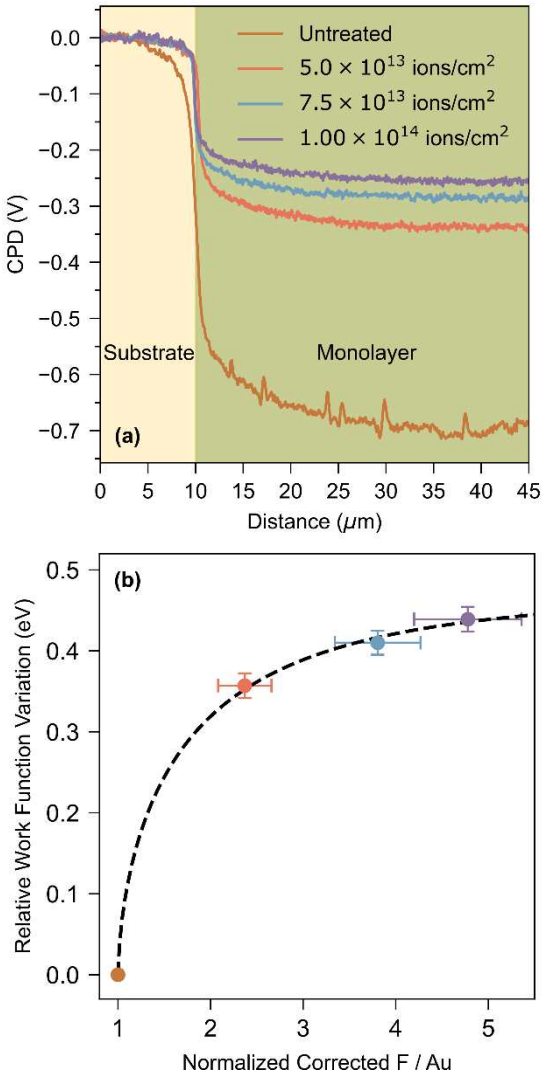

Figure 8 – (a) KPFM line scans across the substrate/monolayer edge for different functionalization densities. (b) Relation between the increase in the functionalization density (proportional to corrected F/Au), and the increase in work function relative to the control sample. Vertical error bars represent the propagated noise contribution to the variation. Horizontal error bars represent uncertainty from the quantification process. Dotted lines represent trend lines.

Figure 8a shows the results of the KPFM measurements. The curves show a progressive increase in the monolayer's CPD, proportional to the work function, associated with a higher pre-treatment fluence and hence a higher functionalization density. The results align very well with literature studies, which claim that functionalization with electron-withdrawing molecules causes p-doping of the material, and therefore an increase in the material's work function [56,57]. In particular, the ΔCPD for 0,

330 $5.0x10^{13}$ ions/cm^2, $7.5x10^{13}$ ions/cm^2, and $1.00x10^{14}$ ions/cm^2 are respectively -0.693 V ± 0.014 V, -
331 0.336 V ± 0.006 V, -0.283 V ± 0.005 V, and -0.254 V ± 0.006 V. These findings provide clear evidence
332 that ion beam treatment enables deterministic control over the physicochemical properties of
333 monolayer MoS_2. Notably, the most pronounced incremental change in work function occurs at the
334 lowest ion fluence, corresponding to an approximately twofold increase in functionalization density
335 relative to the untreated monolayer (Figure 8b). At higher fluences, further increases in
336 functionalization density are accompanied by smaller additional work-function shifts. These results
337 indicate that low-fluence ion-beam defect engineering, followed by thiol functionalization, can
338 provide substantial control over the physicochemical properties of monolayer MoS_2 while reducing
339 ion beam exposure-induced lattice degradation. This work shows that the basal-plane reactivity of
340 Au-supported monolayer MoS_2 can be tuned by Ar ion beam exposure. XPS analysis reveals a fluence-
341 dependent increase in sulfur-deficient Mo environments, which correlates with enhanced chemical
342 reactivity. Higher defect concentrations accelerate oxidation of the monolayer under ambient
343 conditions, indicating that ion beam-generated vacancies reduce the kinetic stability of the otherwise
344 relatively inert basal plane. In parallel, reaction with PFDT under inert conditions produces a fluence-
345 dependent increase in the F 1s signal and changes in the Mo 3d line shape, consistent with increased
346 molecular uptake at sulfur-deficient sites. Because irradiation can also create holes in the monolayer,
347 part of the fluorine signal may originate from PFDT self-assembled monolayers formed on exposed
348 Au regions. An attenuation-based XPS model was built and used to estimate and subtract this Au-
349 related contribution, providing a more reliable quantification. After correction, the MoS_2-associated
350 fluorine signal, used as a proxy for functionalization density, increases by up to a factor of 4.8 ± 0.6
351 relative to untreated monolayers. The comparison between the results on the stability of the
352 functionalized material for more than one month and the results from air oxidation strongly supports
353 that the functionalization passivates the vacancies, as the reactive sites generated from the ion beam

are quenched by the presence of thiols on the vacancies. The KPFM results, complemented by the XPS quantification, highlight the efficacy of fine defect control via low-fluence ion exposure, proving that a substantial modulation of the physicochemical properties can be achieved while minimizing the lattice degradation detected from the Raman measurements. The latter phenomenon remains a key limitation, as it may compromise electronic devices. Future work should therefore focus on identifying irradiation conditions that maximize sulfur-vacancy generation while minimizing structural damage. In particular, systematic studies using different ion species, ion energies, incidence angles, and substrates will be required to control the process in a reproducible and industrially compatible way. With such optimization, ion beam-enabled functionalization could provide a solvent-free and patternable route for tailoring the surface chemistry of monolayer MoS_2.

Methods Natural molybdenite crystals (MoS_2) were purchased from 2D Semiconductors Inc. (Phoenix, AZ, USA). 1*H*,1*H*,2*H*,2*H*-perfluorodecanethiol (97% purity) was obtained from Sigma-Aldrich and used as received without further purification. Silicon wafers with thermally grown silicon dioxide (SiO_2/Si) thicknesses of either 90 nm or 100 nm were used as substrates. To investigate single-layer differences while maintaining a large analysis area for optimal signal, gold-assisted exfoliation has been used to obtain reproducible, large monolayer flakes, following the technique described by Velický et al., who first outlined the possibility of producing these samples [37]. A magnetron sputter coater (Q150T S Plus, Quorum Technologies Ltd., UK) was used to sequentially sputter-coat the SiO_2 substrates with Ni (10 nm) and Au (30 nm). Immediately after the deposition, MoS_2 flakes were mechanically exfoliated from bulk crystals using Kapton tape and transferred onto the freshly prepared substrates. The samples were introduced into the load lock of the XPS instrument within 15 minutes after exfoliation to minimize ambient surface contamination before the UHV experiments. Following exfoliation, each sample was examined by optical microscopy to identify a suitable monolayer flake for treatment and analysis. This was done by selecting the flakes with the lowest

optical contrast on the sample. After transfer into the analyzer chamber of the instrument, the sample position was aligned using x-ray-induced secondary electron microscopy (SXI) (Supplementary Figure 1 in SI). X-ray photoelectron spectroscopy (XPS) measurements were performed on each selected flake before ion beam exposure, immediately after ion beam exposure, and after each subsequent reaction step. Before each experiment, the Mo/Au ratio of the pristine samples was measured and used to calculate the thickness and confirm the monolayer nature through the following equation, assuming full coverage under the analysis spot:

$$\frac{I_{Mo_{3d}}\sigma_{Au_{4f}}}{I_{Au_{4f}}\sigma_{Mo_{3d}}} = \frac{Mo}{Au}(C) = \frac{C\rho_{Mo,MoS_2}\lambda_{Mo_{3d},MoS_2}\left(1 - e^{-\frac{t_{MoS_2}}{\lambda_{Mo_{3d},MoS_2}\cos(\alpha)}}\right)}{C\rho_{Au}\lambda_{Au_{4f},Au}\left(e^{-\frac{t_{MoS_2}}{\lambda_{Au_{4f},MoS_2}\cos(\alpha)}}\right) + (1-C)\rho_{Au}\lambda_{Au_{4f},Au}} \quad (Equation\ 3)$$

C = MoS_2 fractional coverage

$\rho_{Mo,MoS2}$ = Atomic density of molybdenum in MoS_2 [atoms/cm^3]

$\lambda_{Mo3d,MoS2}$ = Effective Attenuation Length of Mo_{3d} photoelectrons through the MoS_2 monolayer [nm]

t_{MoS2} = Thickness of the MoS_2 monolayer [nm]

ρ_{Au} = Atomic density of gold [atoms/cm^3]

$\lambda_{Au4f,Au}$ = Effective Attenuation Length of Au_{4f} photoelectrons through the gold substrate [nm]

$\lambda_{Au4f,MoS2}$ = Effective Attenuation Length of Au_{4f} photoelectrons through the MoS_2 monolayer [nm]

The average thickness calculated from the XPS spectra of the pristine samples is 0.6 ± 0.1 nm, in good agreement with the literature [58,59]. This method was validated by comparison with Raman measurements (in SI), which are commonly used as a standard to estimate the thickness of supported MoS_2 flakes. Spectra were acquired using an 1800 lines/mm grating. The effective MoS_2 coverage after ion beam exposure was calculated using the Mo/Au ratio through the same attenuation model as for the pristine monolayers, by fixing the MoS_2 thickness at t_{MoS2} = 0.6 nm. This approach accounts for the partial removal of monolayer regions during ion beam exposure. The model was validated by

400 comparison with the Raman spectra of pristine MoS_2 (Figure 8), which present the typical features of
401 a monolayer [37]. For ambient-air oxidation experiments, ion beam-treated samples were removed
402 from the vacuum system and placed on a laboratory bench under ambient conditions for the selected
403 exposure time. Relative humidity during the experiments varied between approximately 20% and
404 40%. After exposure, the samples were reintroduced into the XPS system and analyzed without
405 further treatment. Since humidity could affect oxidation and adsorption kinetics, it was treated as a
406 potential source of experimental variability. The oxidation experiments were performed over four
407 months using independent batches of freshly exfoliated monolayer samples. Each data point,
408 corresponding to a specific combination of ion fluence and air exposure time, was obtained using
409 three samples that were processed as a batch and exposed to ambient air simultaneously. Therefore,
410 the three replicate samples for each data point experienced the same humidity history. The standard
411 deviation of each point mainly reflects sample-to-sample differences, XPS quantification uncertainty,
412 and variations in the ion beam-induced defect density, for example due to ion current fluctuations,
413 rather than variations in humidity. Day-to-day changes in humidity contribute instead to the scatter
414 between independently measured batches. Because these humidity variations were not
415 systematically correlated with ion fluence or exposure time, they are expected to increase the
416 experimental scatter but not to generate an artificial fluence-dependent oxidation trend. Thiol
417 reactivity experiments were performed using a procedure similar to the one described by Bertolazzi
418 et al. [60]. In their study, they created vacancies by using low fluences of Ar ions and healed them by
419 exposure to alkanethiols, proving successful restoration of the electronic properties. Ion beam-
420 treated samples were transferred directly to an Ar-filled glovebox with less than 0.1 ppm of oxygen
421 and water by using a sealed transfer vessel, thereby preventing exposure to ambient atmosphere
422 prior to the reaction. Samples were then introduced into a glass vessel preheated to 70 °C for 1 hour
423 with *1H,1H,2H,2H*-Perfluor-1-decanethiol (PFDT) (100 µL) to saturate the reaction chamber. Following

424 the reaction time, the samples were annealed at 70 °C for 1 hour and transferred back to the XPS
425 instrument for analysis using the same air-free transfer procedure. X-ray photoelectron spectra were
426 collected using a Physical Electronics PHI VersaProbe III equipped with a hemispherical energy
427 analyzer, a scanning monochromatic Al Kα X-ray source (1486.6 eV), and a standard monatomic Ar^+
428 ion gun. Data were acquired with a focused X-ray beam (20, 50, or 100 µm diameter) at a base
429 pressure below $1x10^{-8}$ mbar and a take-off angle of 45°. The Ar^+ ion gun was operated at an incidence
430 angle of 59°, with an acceleration voltage of 500 V. Beam alignment and ion current were verified
431 before each batch of experiments using a Faraday cup, and the gun was set in blank mode for 1 hour
432 before each experiment to stabilize the current. Fluence was calculated according to the following
433 equation:

434 $$F = \frac{i\,t}{q\,e\,A} \quad (Equation\ 4)$$

435 F = Fluence [ions/cm^2]

436 i = Current [A=C/s]

437 t = Time [s]

438 q = Ion charge

439 e = Elementary charge = $1.602x10^{-19}$ C

440 A = Area [cm^2]

441 XPS were analyzed with the software CasaXPS. Peak fitting of the Mo 3d XPS spectra has been
442 performed by constraining peak areas of Mo $3d_{5/2}$ and Mo $3d_{3/2}$ using a 3:2 branching ratio and a 3.13
443 eV spin-orbit splitting. For semiconducting or conducting phases, the Coster-Kronig effect leads to an
444 increased FWHM of the lower spin-orbit component; accordingly, a difference of 0.18 eV was imposed
445 between spin-orbit components associated with MoS_2 and reduced molybdenum (rMo). In contrast,
446 Mo oxides (MoO_x) do not exhibit the Coster-Kronig effect, so their spin-orbit components were
447 constrained to have identical FWHM. Mo 3d peaks associated with molybdenum oxide were fitted

using a Gaussian-Lorentzian (GL(80)) function, while pristine MoS_2 and rMo components were fitted using an asymmetric Lorentzian (LA(1.4,3,0)) function. All spectra have been charge-referenced by fixing the Au $4f_{7/2}$ peak position at 84 eV. Raman spectra were collected using a confocal Horiba Jobin Yvon LabRAM HR spectrometer equipped with a 532 nm excitation laser and a 100x objective lens (NA = 0.9). Raman spectra were analyzed with the software CasaXPS: background subtraction was performed using a polynomial regression function, while peaks were fitted with a Lorentzian LA(50) function. Surface potential line scans were acquired using the integrated in situ scanning probe microscopy (SPM) module inside a ToF-SIMS instrument (ToF-SIMS M6 Plus, IONTOF GmbH, Münster, Germany) under UHV conditions (base pressure $1x10^{-9}$ mbar). Measurements were performed in amplitude-modulation (AM) KPFM mode across the monolayer MoS_2/Au boundary using CDT-FMR tips with a nominal spring constant of 6.2 N/m and a nominal resonance frequency of 105 kHz. Line scans were performed at a constant scan speed of 2000 nm/s, with an AC excitation voltage of 0.35 V applied to the stage. The potential difference was multiplied by -1 to make it proportional to the sample's work function. The local work function difference was determined by referencing the line scan profiles to the adjacent functionalized Au substrate, set to 0 V. The ΔCPD has been calculated considering the range 0-5 µm for the substrate and the range 25-45 µm for the monolayer flake.

Author contributions

F.L. conceived the idea and designed the experiments. F.L. prepared the samples and performed the XPS measurements with assistance from M.S.. F.F. performed the KPFM measurements. M.O. performed the Raman measurements. F.L. analyzed the data. M.V. provided resources and secured funding for the Raman spectrometer. A.F. secured funding for the project and the XPS instrumentation and supervised the study. F.L. wrote the manuscript with critical input from all authors. All authors reviewed and approved the final manuscript.

Acknowledgments

The Austrian Research Promotion Agency (FFG) is gratefully acknowledged for funding both the XPS infrastructure (FFG project number: 884672) and the ToF SIMS instrument IONTOF M6 Plus (FFG project number: 902876). This research was funded in part by the Austrian Science Fund (FWF) [10.55776/DOC142] (TU-DX: Towards Applications of 2D Materials).

Competing interests

All authors declare no financial or non-financial competing interests.

Data availability

The datasets analyzed during the current study are available in the TU Wien Research Data repository (DOI:10.48436/hf8rn-tme55).

References

1. Mak, K. F., Lee, C., Hone, J., Shan, J. & Heinz, T. F. Atomically Thin MoS 2 : A New Direct-Gap Semiconductor. *Phys. Rev. Lett.* **105**, 136805 (2010).
2. Radisavljevic, B., Radenovic, A., Brivio, J., Giacometti, V. & Kis, A. Single-layer MoS2 transistors. *Nat. Nanotechnol.* **6**, 147–150 (2011).
3. Wang, Q. H., Kalantar-Zadeh, K., Kis, A., Coleman, J. N. & Strano, M. S. Electronics and optoelectronics of two-dimensional transition metal dichalcogenides. *Nat. Nanotechnol.* **7**, 699–712 (2012).
4. Chhowalla, M. *et al.* The chemistry of two-dimensional layered transition metal dichalcogenide nanosheets. *Nat. Chem.* **5**, 263–275 (2013).
5. Late, D. J. *et al.* Sensing Behavior of Atomically Thin-Layered MoS_2 Transistors. *ACS Nano* **7**, 4879–4891 (2013).
6. Perkins, F. K. *et al.* Chemical Vapor Sensing with Monolayer MoS_2. *Nano Lett.* **13**, 668–673 (2013).

494 7. Li, H. *et al.* Fabrication of Single- and Multilayer MoS_2 Film-Based Field-Effect Transistors for
495 Sensing NO at Room Temperature. *Small* **8**, 63–67 (2012).
496 8. Bollinger, M. V. *et al.* One-Dimensional Metallic Edge States in MoS 2. *Phys. Rev. Lett.* **87**, 196803
497 (2001).
498 9. Lauritsen, J. V. *et al.* Size-dependent structure of MoS2 nanocrystals. *Nat. Nanotechnol.* **2**, 53–58
499 (2007).
500 10. Hinnemann, B. *et al.* Biomimetic Hydrogen Evolution: MoS_2 Nanoparticles as Catalyst for
501 Hydrogen Evolution. *J. Am. Chem. Soc.* **127**, 5308–5309 (2005).
502 11. Jaramillo, T. F. *et al.* Identification of Active Edge Sites for Electrochemical H_2 Evolution from MoS_2
503 Nanocatalysts. *Science* **317**, 100–102 (2007).
504 12. Komsa, H.-P. & Krasheninnikov, A. V. Native defects in bulk and monolayer MoS 2 from first
505 principles. *Phys. Rev. B* **91**, 125304 (2015).
506 13. Hong, J. *et al.* Exploring atomic defects in molybdenum disulphide monolayers. *Nat. Commun.* **6**,
507 6293 (2015).
508 14. Zhou, W. *et al.* Intrinsic Structural Defects in Monolayer Molybdenum Disulfide. *Nano Lett.* **13**,
509 2615–2622 (2013).
510 15. Vancsó, P. *et al.* The intrinsic defect structure of exfoliated MoS2 single layers revealed by
511 Scanning Tunneling Microscopy. *Sci. Rep.* **6**, 29726 (2016).
512 16. Komsa, H.-P. *et al.* Two-Dimensional Transition Metal Dichalcogenides under Electron Irradiation:
513 Defect Production and Doping. *Phys. Rev. Lett.* **109**, 035503 (2012).
514 17. Lin, Z. *et al.* Defect engineering of two-dimensional transition metal dichalcogenides. *2D Mater.* **3**,
515 022002 (2016).
516 18. Quirós-Ovies, R., Han, B. & Samorì, P. Covalent Functionalization of 2D Semiconductors: A
517 Roadmap to Advanced Electronic Devices. *Adv. Funct. Mater.* **n/a**, e78433.

19. Gupta, S., Johnston, A. & Khondaker, S. Surface and Physical Properties Modifications of Electron Beam-Irradiated Monolayer MoS2-Au Heterointerface at Nanoscale. *J. Electron. Mater.* **52**, 1331–1346 (2023).
20. Fox, D. S. *et al.* Nanopatterning and Electrical Tuning of MoS_2 Layers with a Subnanometer Helium Ion Beam. *Nano Lett.* **15**, 5307–5313 (2015).
21. Fekri, Z. *et al.* Tuning the Electronic Characteristics of Monolayer MoS2-Based Transistors by Ion Irradiation: The Role of the Substrate. *Adv. Electron. Mater.* **10**, 2400037 (2024).
22. Komsa, H.-P., Kurasch, S., Lehtinen, O., Kaiser, U. & Krasheninnikov, A. V. From point to extended defects in two-dimensional MoS 2 : Evolution of atomic structure under electron irradiation. *Phys. Rev. B* **88**, 035301 (2013).
23. Mignuzzi, S. *et al.* Effect of disorder on Raman scattering of single-layer Mo S 2. *Phys. Rev. B* **91**, 195411 (2015).
24. Zhao, Y., Ishiguro, Y. & Takai, K. Effect of low-energy ion-beam irradiation on the structure and electron transport of monolayer MoS2. *Nucl. Instrum. Methods Phys. Res. Sect. B Beam Interact. Mater. At.* **543**, 165095 (2023).
25. Daniel, L. *et al.* In situ Raman study on sulfur vacancies in monolayer MoS2. *2D Mater.* **13**, 025033 (2026).
26. Laudani, F. *et al.* Ion beam-induced MoS2 surface modification: An XPS study of Ar+ and Ar Gas Cluster Ion Beam treatments. *Appl. Surf. Sci.* **753**, 168426 (2027).
27. Rahman, Md. H., Chowdhury, E. H. & Hong, S. High temperature oxidation of monolayer MoS2 and its effect on mechanical properties: A ReaxFF molecular dynamics study. *Surf. Interfaces* **26**, 101371 (2021).
28. Szoszkiewicz, R., Rogala, M. & Dąbrowski, P. Surface-Bound and Volatile Mo Oxides Produced During Oxidation of Single MoS2 Crystals in Air and High Relative Humidity. *Materials* **13**, 3067 (2020).

29. Nan, H. *et al.* Strong Photoluminescence Enhancement of MoS_2 through Defect Engineering and Oxygen Bonding. *ACS Nano* **8**, 5738–5745 (2014).
30. Pető, J. *et al.* Spontaneous doping of the basal plane of MoS2 single layers through oxygen substitution under ambient conditions. *Nat. Chem.* **10**, 1246–1251 (2018).
31. Nguyen, D. K. *et al.* Tuning MoSO monolayer properties for optoelectronic and spintronic applications: effect of external strain, vacancies and doping. *RSC Adv.* **11**, 35614–35623 (2021).
32. Knirsch, K. C. *et al.* Basal-Plane Functionalization of Chemically Exfoliated Molybdenum Disulfide by Diazonium Salts. *ACS Nano* **9**, 6018–6030 (2015).
33. Voiry, D. *et al.* Covalent functionalization of monolayered transition metal dichalcogenides by phase engineering. *Nat. Chem.* **7**, 45–49 (2015).
34. Presolski, S. & Pumera, M. Covalent functionalization of MoS2. *Mater. Today* **19**, 140–145 (2016).
35. Chen, X., Berner, N. C., Backes, C., Duesberg, G. S. & McDonald, A. R. Functionalization of Two-Dimensional MoS2: On the Reaction Between MoS2 and Organic Thiols. *Angew. Chem.* **128**, 5897–5902 (2016).
36. Li, Q. *et al.* Towards a Comprehensive Understanding of the Reaction Mechanisms Between Defective MoS2 and Thiol Molecules. *Angew. Chem. Int. Ed.* **56**, 10501–10505 (2017).
37. Velický, M. *et al.* Strain and Charge Doping Fingerprints of the Strong Interaction between Monolayer MoS2 and Gold. *J. Phys. Chem. Lett.* **11**, 6112–6118 (2020).
38. Hanušová, M. *et al.* Hybridization Directionality Governs the Interaction Strength between MoS2 and Metals. *Nano Lett.* **25**, 12995–13002.
39. Xu, H. *et al.* Two-Dimensional MoS2: Structural Properties, Synthesis Methods, and Regulation Strategies toward Oxygen Reduction. *Micromachines* **12**, 240 (2021).
40. Amba Sankar, K. N. *et al.* Renewable synthesis of MoO3 nanosheets via low temperature phase transition for supercapacitor application. *Sci. Rep.* **14**, 20503 (2024).
41. Lince, J. R. Schottky-barrier formation on a covalent semiconductor without Fermi-level pinning: The metal-MoS2(0001) interface. *Phys. Rev. B* **36**, 1647–1656 (1987).

42. Liu, Y. & Shen, L. From Langmuir Kinetics to First- and Second-Order Rate Equations for Adsorption. *Langmuir* **24**, 11625–11630 (2008).
43. KC, S., Longo, R. C., Wallace, R. M. & Cho, K. Surface oxidation energetics and kinetics on MoS2 monolayer. *J. Appl. Phys.* **117**, 135301 (2015).
44. Nuzzo, R. G. & Allara, D. L. Adsorption of bifunctional organic disulfides on gold surfaces. *J. Am. Chem. Soc.* **105**, 4481–4483 (1983).
45. Nuzzo, R. G., Zegarski, B. R. & Dubois, L. H. Fundamental studies of the chemisorption of organosulfur compounds on gold(111). Implications for molecular self-assembly on gold surfaces. *J. Am. Chem. Soc.* **109**, 733–740 (1987).
46. Love, J. C., Estroff, L. A., Kriebel, J. K., Nuzzo, R. G. & Whitesides, G. M. Self-Assembled Monolayers of Thiolates on Metals as a Form of Nanotechnology. *Chem. Rev.* **105**, 1103–1170 (2005).
47. Seah, M. P. Simple universal curve for the energy-dependent electron attenuation length for all materials. *Surf. Interface Anal.* **44**, 1353–1359 (2012).
48. Frey, S. *et al.* Structure of self-assembled monolayers of semifluorinated alkanethiols on gold and silver substrates. *Isr. J. Chem.* **40**, 81–97 (2000).
49. Alves, C. A. & Porter, M. D. Atomic force microscopic characterization of a fluorinated alkanethiolate monolayer at gold and correlations to electrochemical and infrared reflection spectroscopic structural descriptions. *Langmuir* **9**, 3507–3512 (1993).
50. Trasatti, S. & Petrii, O. A. Real surface area measurements in electrochemistry. *Pure Appl. Chem.* **63**, 711–734 (1991).
51. Hamelin, A. Cyclic voltammetry at gold single-crystal surfaces. Part 1. Behaviour at low-index faces. *J. Electroanal. Chem.* **407**, 1–11 (1996).
52. Hamelin, A. & Martins, A. M. Cyclic voltammetry at gold single-crystal surfaces. Part 2. Behaviour of high-index faces. *J. Electroanal. Chem.* **407**, 13–21 (1996).

53. Ziewer, J. *et al.* Strain-Induced Decoupling Drives Gold-Assisted Exfoliation of Large-Area Monolayer 2D Crystals. *Adv. Mater.* **37**, 2419184 (2025).
54. Huang, X. *et al.* Raman spectra evidence for the covalent-like quasi-bonding between exfoliated MoS2 and Au films. *Sci. China Inf. Sci.* **64**, 140406 (2021).
55. Gollner, C. *et al.* Interfacial Control of Hot-Carrier Extraction and Photostability in Two-Dimensional Materials. *ACS Nano* **20**, 26205–26214 (2026).
56. Sim, D. M. *et al.* Controlled Doping of Vacancy-Containing Few-Layer MoS2 via Highly Stable Thiol-Based Molecular Chemisorption. *ACS Nano* **9**, 12115–12123 (2015).
57. Han, B., Gali, S. M., Dai, S., Beljonne, D. & Samorì, P. Isomer Discrimination via Defect Engineering in Monolayer MoS2. *ACS Nano* **17**, 17956–17965 (2023).
58. Shi, Z.-T. *et al.* Chemical vapor deposition growth and transport properties of MoS2–2H thin layers using molybdenum and sulfur as precursors. *Rare Met.* **41**, 3574–3578 (2022).
59. Nie, Y. *et al.* Transmission-Matrix Quantitative Phase Profilometry for Accurate and Fast Thickness Mapping of 2D Materials. *ACS Photonics* **10**, 1084–1092 (2023).
60. Bertolazzi, S. *et al.* Engineering Chemically Active Defects in Monolayer MoS2 Transistors via Ion-Beam Irradiation and Their Healing via Vapor Deposition of Alkanethiols. *Adv. Mater.* **29**, 1606760 (2017).

Supplementary Files

This is a list of supplementary files associated with this preprint. Click to download.

- SupplementaryInformation.docx